SOL TRANSPORT AND DETACHMENT IN ALTERNATIVE DIVERTOR CONFIGURATIONS IN TCV L- AND H-MODE PLASMAS

C. THEILER[1], J. HARRISON[2], O. FEVRIER[1], H. DE OLIVEIRA[1], M. BERNERT[3], J.A. BOEDO[4], B. DUVAL[1], N. FEDORCZAK[5], A. FIL[6], D. GALASSI[1], A. GALLO[7], P. INNOCENTE[8], B. LABIT[1], B. LINEHAN[9], B. LIPSCHULTZ[6], R. MAURIZIO[1], B. MUMGAARD[9], A. PEREK[10], H. REIMERDES[1], U. SHEIKH[1], A.J. THORNTON[2], C.K. TSUI[1,4], K. VERHAEGH[1,6], N. VIANELLO[8], W.A.J. VIJVERS[10], M. WENSING[1], C. WÜTHRICH[1] AND THE TCV TEAM[11] AND THE EUROFUSION MST1 TEAM[12]
[1]Ecole Polytechnique Fédérale de Lausanne (EPFL), Swiss Plasma Center (SPC), Lausanne, Switzerland, [2]CCFE, Culham Science Centre, Abingdon, United Kingdom, [3]Max Planck Institut für Plasmaphysik, Garching, Germany, [4]University of California-San Diego, La Jolla, USA, [5]IRFM, CEA-Cadarache, France, [6]York Plasma Institute, University of York, York, United Kingdom, [7]Aix-Marseille Univ, CNRS, PIIM, Marseille, France, [8]Consorzio RFX, Padova, Italy, [9]MIT, Plasma Science and Fusion Center, Cambridge, USA, [10]DIFFER, Eindhoven, Netherlands, [11]See the author list of Coda et al., Nucl. Fusion 57 (2017) 102011, [12]See the author list of H. Meyer et al., Nucl. Fusion 57 (2017) 102014
Corresponding author: christian.theiler@epfl.ch

Abstract

The effect of magnetic geometry on scrape-off layer (SOL) transport and detachment behaviour is investigated on the TCV tokamak with the goal of assessing the potential benefits of alternative divertor solutions and for the validation of theoretical models. Following an overview of recent progress in L-mode plasmas, the current status of detachment in H-mode conventional and alternative geometries on TCV is presented. The clearest signs of detachment of the outer target inter-ELM strikepoint have been obtained so far at intermediate current (q_{95}=3.9) and with nitrogen seeding. A strong cooling of the outer target, a clear drop and change in shape of the j_{sat} profile and an upstream movement of the NII and CIII emission region from the target to the X-point are observed. Geometrical modifications of these plasmas so far include a variation in outer target major radius by 40% and a factor four variation in outer target poloidal flux expansion. First observations in these plasmas include an approximately 20% slower movement of the impurity emission front with increasing target radius. Increasing the outer target poloidal flux expansion instead shows indications of more resilience of the H-mode regime to the injection of nitrogen and a stronger reduction in the target ion flux. While the radiation in the outer leg increases with flux expansion, similarly as for L-mode seeding and fuelling ramps, the relative radiation levels in this region are substantially lower than for the L-mode experiments. Indeed, even before seeding, almost all of the inter-ELM radiation is located around the X-point and further upstream, and thus away from the region where magnetic geometry is modified. To further assess the effect of magnetic geometry on H-mode detachment on TCV likely requires going to higher SOL power levels or to the baffled divertor configuration scheduled for mid-2019.

1. INTRODUCTION

Over the past years, a number of alternative divertor geometries have been proposed to address the outstanding issue of safe power exhaust in future reactors. The proposed alternatives include advanced magnetic geometries, such as the Snowflake, the X-Divertor, the Super-X Divertor, and the X-Point Target Divertor, as well as optimized divertor plate geometries and neutral baffling (see [1] for a recent review). These approaches aim at reducing peak target heat fluxes and erosion and improving edge-core compatibility by facilitating access to detachment (e.g. at reduced impurity seeding rates), increasing divertor radiation levels, and providing improved control of the detachment front.
The unique shaping capabilities of the TCV tokamak [2] at EPFL together with its extensive diagnostic coverage is leveraged to explore the effect of magnetic geometry on scrape-off layer (SOL) transport and detachment behaviour. Here, the goal is to assess the potential benefits of various alternative divertor geometries and to validate theoretical models [3-5]. In the first section of this paper, we present a short overview of recent progress in the understanding of transport and detachment in alternative divertor geometries in TCV L-mode plasmas. Recent attempts to extend these studies to the more challenging H-mode conditions are presented subsequently.

2. PROGRESS ON DIVERTOR TRANSPORT AND DETACHMENT IN TCV L-MODE PLASMAS

Since the work on detachment in alternative divertor geometries in TCV L-mode plasmas presented in [3,5,6], significant progress has been achieved in the understanding of SOL transport, detachment and associated modelling, with the main results briefly summarized in this section.
New insights on the geometry dependence of the divertor power sharing P_{in}/P_{out}, the heat flux decay length lambda_q, and the divertor spreading factor S were obtained in attached TCV L-mode experiments [7,8]. Increasing midplane to outer target connection length via increased flux expansion and divertor leg length was

found to increase P_{in}/P_{out}. This behaviour is explained by a reduced thermal conductance of the outer divertor with increasing connection length [9]. Within its range of validity, the power sharing model in [9], which also includes effects of a change in major radius along the magnetic field, is a useful tool to investigate the dependence of P_{in}/P_{out} on divertor geometry. The increase in flux expansion further showed little effect on lambda_q and resulted in a *decrease* of the upstream mapped S. The latter implies that divertor heat flux spreading is more effective the smaller the flux expansion. A different behaviour was observed in the leg length scan. lambda_q increases approximately as the square root of the divertor leg length, while S displays no systematic trend. TOKAM3X three-dimensional turbulence simulations of the leg length scan are in qualitative agreement with the experiment and can explain observations by a strongly asymmetric (ballooning) transport at and below the X-point [8].
Evidence for increased cross-field transport in the region of low poloidal field has been obtained in Snowflake geometries [10]. With an additional X-point in the low-field side SOL, lambda_q near the X-point increases by a factor two with respect to a comparable single-null plasma. This was inferred from the power to the outermost strikepoint as a function of the distance between the two X-points. First TCV edge transport simulations with drifts included show that divertor dynamics are further complicated by significant ExB drifts, in some cases causing double-peaked heat flux footprints at the inner strikepoint [11].

Novel spectroscopic techniques provide a detailed picture of particle and power balance along the outer divertor leg and the detachment process. The drop in target ion current and access to detachment on TCV is found to be caused by a reduction of the divertor ionization source. In agreement with analytical predictions, this reduction is driven by a reduction in the power available for ionization and an increase in the energy cost per ionization with decreasing T_e. Volume recombination, on the contrary, only becomes a significant contributor at high levels of detachment [12,13]. SOLPS modeling confirms these observations [14] and simulations are being extended to Super-X geometries [15] to shed light on the experimentally observed insensitivity of the detachment behaviour on total flux expansion in TCV Super-X geometries.
The effect of connection length on upstream SOL profiles and fluctuations has been investigated in density ramp experiments over a range of outer target flux expansion [16]. The formation of an upstream density shoulder could be related to the blob size, which increases with density. However, no influence on connection length was observed, indicating that divertor normalized collisionality is not sufficient to obtain density shoulder formation.
A large database of reciprocating probe data has been used to validate blob velocity scalings in the TCV SOL [17]. Most blobs on TCV are found to populate the resistive ballooning regime, where their radial velocity has little or no dependence on collisionality and, hence, on connection length. A detailed comparison of L-mode detachment via either density ramps or nitrogen seeding on TCV was performed in [18]. While comparable levels of detachment were achievable, the evolution of the upstream density profile is vastly different. The formation of the upstream density shoulder coincides with the onset of detachment in the density ramp experiment, while detachment occurs without density shoulder formation in case of nitrogen seeding.

3. EXTENSION OF DETACHMENT STUDIES TO TCV H-MODE PLASMAS

Within High Level Topic 24 of the 2017-2018 EUROfusion MST1 campaign on TCV, experimental work has focused on extending alternative divertor detachment studies to neutral beam heated H-mode plasmas. In order to determine the access condition to H-mode as a function of geometry, neutral beam power ramps were conducted in Standard, X-, Super-X, and Snowflake Minus geometries [19]. These experiments were performed at 210 kA with a line-averaged density of approx. $5x10^{19}m^{-3}$, corresponding to the density range where the L-H threshold is expected to have a minimum based on previous studies [20]. These experiments revealed a weak dependence (<10%) of divertor geometry on the H-mode power threshold and in all divertor geometries, a transition to an ELMy regime was observed. Ref. [19] further presents an extensive assessment of the explored parameter space for H-mode detachment on TCV using fuelling and nitrogen seeding. This includes a detailed power balance in ELMfree and ELMy H-mode plasmas and an assessment of the achieved target heat and particle flux reductions, the dynamics of impurity line radiation in the divertor volume, and the effect of fuelling and seeding on the repartition of radiated power and core confinement.

Here, we present observations from detachment experiments in ELMy H-mode for the configurations shown in Fig. 1. The configuration in Fig. 1(a) corresponds to a 210 kA discharge with intermediate outer target flux expansions, see Fig. 1(g), which transitions into a stationary ELMy regime following injection of 1MW of beam power. By injecting nitrogen from the (toroidally localized) position indicated in Fig. 1(a), this scenario has shown the clearest signs of inter-ELM detachment of the outer target to date, as discussed in Sec. 3.1. As this scenario has not always been reliable to reproduce, a more robust scenario, whose main change is a lower plasma current (170kA), is used to explore the effect of divertor geometry on detachment. Previous studies in this 170kA scenario focused on the effect of seeding and fuelling on the pedestal structure [21], and it is

extended here to a range of outer target flux expansion, Fig. 1(b)-(d), and target major radius, Fig. 1(e). N_2 seeded detachment studies in these geometries are discussed in Sec. 3.2.

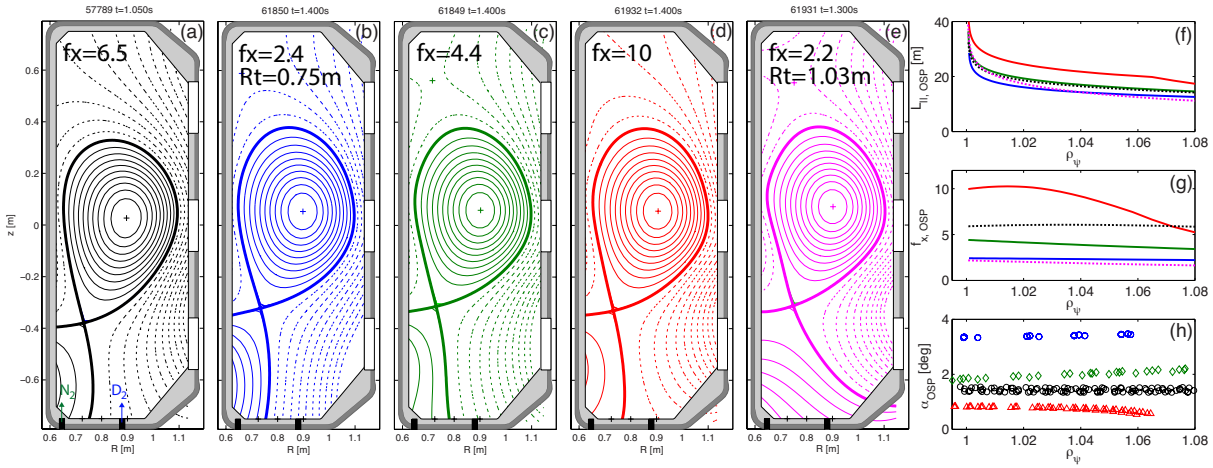

FIG 1: (a)-(e): Equilibrium plots of the ELMy H-mode scenarios investigated in this paper. Scenario (a) has a plasma current of 210kA, while the others are at 170kA. They all feature 1MW of injected beam power. The D_2 fuelling and N_2 seeding locations on the floor are indicated. (f)-(h): Radial profiles of connection length (from outer midplane to outer target), outer target flux expansion, and incidence angle of the magnetic field on the TCV wall tiles.

3.1. Effect of fuelling and seeding on outer target inter-ELM profiles

In this section, we focus on ELMy H-modes in the configuration shown in Fig. 1(a). The plasma has a major radius R_0=0.89m, an on-axis magnetic field of B_0=1.43T, a plasma current of I_p=210kA (q_{95}=3.9), and is run with the ion gradB drift towards the primary X-point, generally termed *forward field direction*. 1MW of injected beam power [22] results in a stationary ELMy discharge with a line-averaged density $\langle n_e \rangle$ of approximately $5\text{x}10^{19}\text{m}^{-3}$ (f_{GW}=0.35). The gas fuelling is cut during the H-mode phase.

To approach detachment in this scenario, both nitrogen seeding and deuterium fuelling from the valves indicated in Fig. 1(a) was explored. In Fig. 2, the effect of seeding on the outer strikepoint is presented, as inferred from the TCV wall-embedded Langmuir Probes (LPs) [23] operated in swept mode. Nitrogen is injected at ~1.01s, as indicted in Fig. 2(b). This reduces the ELM amplitude, as seen from the D-alpha photodiode signal. The latter correlates well with the target ion flux during ELMs, inferred when the LPs are operated in ion saturation mode (not shown), while the core energy loss per ELM does not change significantly with nitrogen. This could be an indication that the ELM energies are more efficiently dissipated in the SOL and divertor in the presence of nitrogen. At ~100ms after the seeding commences, a back-transition to L-mode occurs. To date, no strong attempt has been made to make this seeded scenario more stationary.
In Fig. 2(a), we compare the outer target, inter-ELM j_{sat} profile for the intervals before (red) and after (blue) the start of nitrogen seeding highlighted in Fig. 2(b). This was obtained by averaging the LP current over the 5% lowest voltage values of each sweep cycle and discarding data contaminated by ELMs. It reveals a peaked j_{sat} profile in the absence of nitrogen. The injection of nitrogen results in a significant reduction of j_{sat} in the vicinity of the separatrix, indicative of partial detachment. Consistent with this observation, the total ion flux to the outer strikepoint shown in Fig. 2(c) drops by approximately 40% in response to the seeding. In Fig. 2(e)-(g), we compare the inter-ELM target profiles of density n_e, electron temperature T_e, and ground current J_0 (the probe current density measured when the LP voltage coincides with the voltage of the wall tiles) for a discharge with and without nitrogen seeding and during the time interval highlighted in Fig. 2(d). This was obtained by discarding LP data contaminated by ELMs and averaging over intervals of 40ms to determine the inter-ELM current-voltage characteristics. The profiles reveal a strong cooling of the target plasma, consistent with the onset of detachment, with T_e dropping below 5eV near the separatrix. J_0 also strongly drops due to the nitrogen, while the target density is only weakly affected.

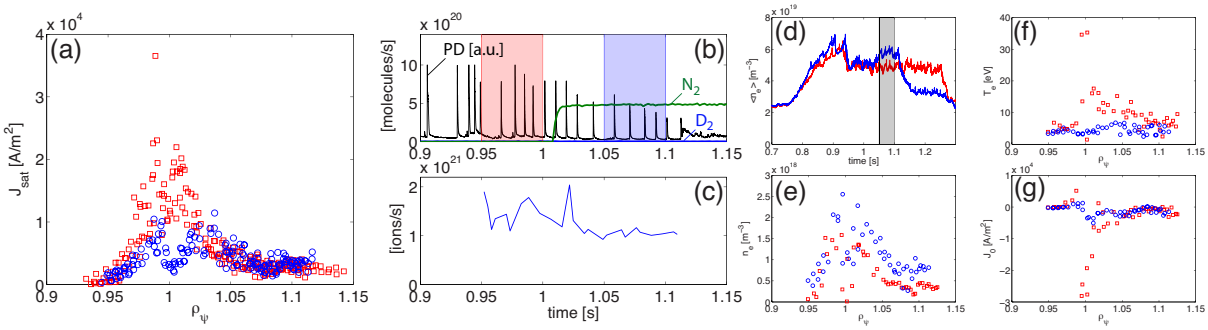

FIG 2: Effect of nitrogen seeding on the outer strikepoint profiles as inferred from the wall LPs for the ELMy H-mode plasma in Fig. 1(a). Subplot (a) shows the j_{sat} profile during the intervals before and after the start of the seeding highlighted in (b) by the shaded regions in corresponding colors. The integral ion flux to the outer strikepoint as a function of time is shown in (c). In (b), the D-alpha photodiode signal is also shown together with the nitrogen (green) and deuterium (blue) injection rate. (e)-(g) compare the target profiles of n_e, T_e, and J_0 during the time interval highlighted in (d) for a discharge with (blue) and without (red) nitrogen seeding.

In a second experiment, a feed-forward D_2 fuelling rate was applied during the ELMy phase, followed by a nitrogen seeding ramp as shown in Fig. 3(b). Plots analogous to the seeding-only case are shown in Fig. 3. During the time when fuelling exceeds the seeding rate (the green interval highlighted in Fig. 3(b)), the outer target remains firmly attached. The target T_e drops, but is still at approximately 15 eV near the separatrix, and the target density has increased. The j_{sat} profile is still peaked near the separatrix and J_0 is large. Profiles characteristic for a partially detached outer divertor are only observed at higher seeding rate. This suggests that strong nitrogen seeding levels are required to detach these ELMy H-mode plasmas.

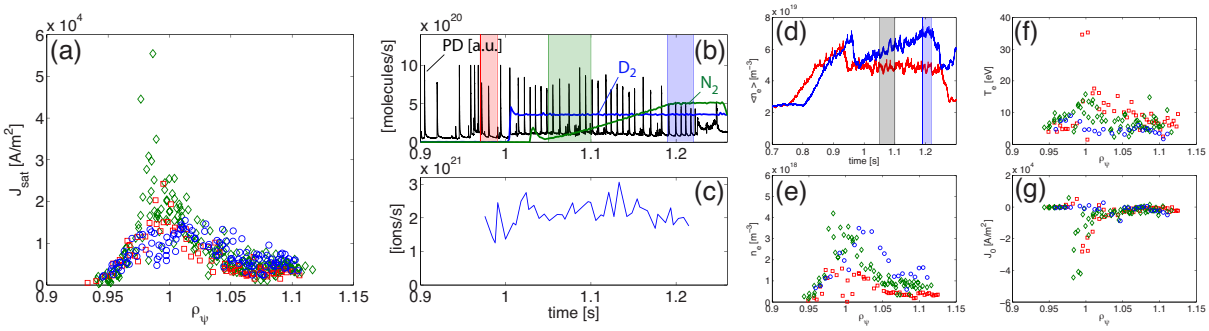

FIG 3: The equivalent to Fig. 2 for a case where both fuelling and seeding is applied during the ELMy phase.

3.2. Nitrogen seeded X- and Super-X ELMy H-mode plasmas

We now discuss first experiments with nitrogen seeding applied to ELMy H-mode in alternative divertor geometries. These scenarios differ from that discussed in the previous section mainly by a reduced current (~170kA). The geometrical modifications, shown in Fig. 1(b)-(e), consist of a scan in outer target poloidal flux expansion f_x (including the X-Divertor) and an increase in outer target major radius R_t (Super-X Divertor). As shown in Fig. 1(g), f_x is varied from approximately 2.4 to 10. The large R_t case (R_t=1.03m) has very similar flux expansion as the small f_x case in Fig. 1(b) with R_t=0.75m. These geometries are similar to those previously investigated on TCV for density ramp experiments in reversed field, 340kA L-mode plasmas, with the following results [3]: The dependence of the detachment threshold on f_x was found to be weak, while a more pronounced j_{sat} roll-over and a deeper detachment with increasing f_x was identified. Additionally, the relatively cold CIII emission front, expected to lie between 3-8eV, and the radiation peak along individual bolometry sightlines were found to recede from the outer target towards the X-point more slowly with increasing fx, indicating an improved controllability of the detachment state. Comparing small and large R_t cases with a 70% variation in R_t, on the contrary, showed no significant differences in the detachment behaviour, contrary to expectations [24].

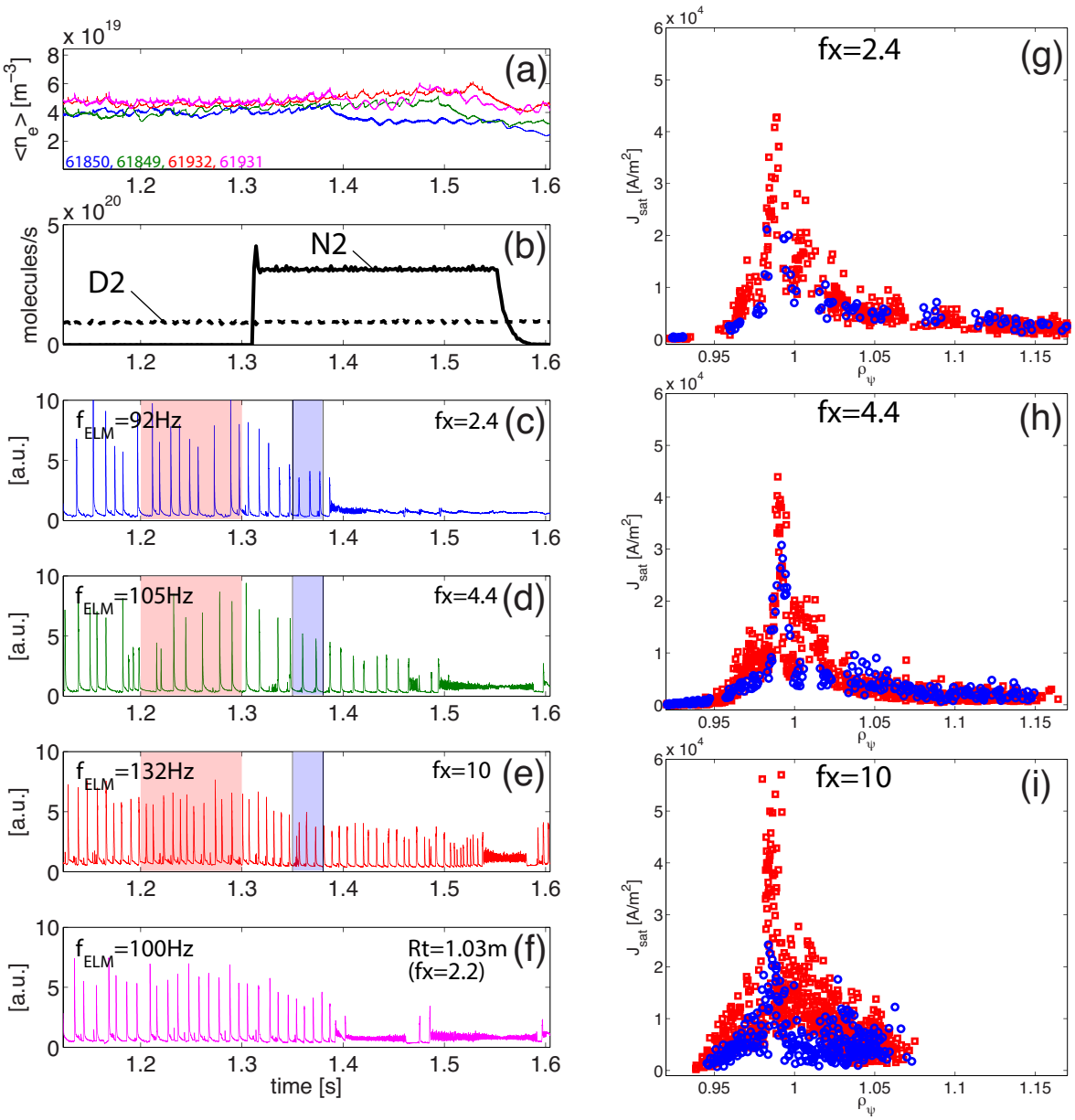

FIG 4: (a) Line-averaged density, (b) fuelling and seeding levels, and (c)-(f) D-alpha time traces for the f_x and R_t scan in Fig. 1 (b)-(e). The average ELM frequency before the seeding start is indicated. (g)-(i) show the inter-ELM j_{sat} profiles for different values of f_x and during the time intervals before (red) and after (blue) the start of the seeding highlighted in (c)-(e) by the shaded region.

Time traces for the ELMy discharges in Fig. 1(b)-(e) are shown in Fig. 4. All have the same fuelling and seeding levels shown in Fig. 4(b). A relatively low, constant fuelling rate is applied throughout to assure a stationary density during the H-mode phase and strong nitrogen seeding is applied at 1.31s. The average ELM frequency prior to the seeding differs with geometry as indicated. However, this quantity is found to depend strongly on $\langle n_e \rangle$, which is not perfectly matched in the different cases, Fig. 4(a) (although the frequency is usually found to drop with density, contrary to the trend in Fig. 4). We observe that the small flux expansion case transitions back to L-mode shortly after the onset of the seeding, in less than 100ms. This back-transition is delayed with increasing f_x, with the seeded ELMy phase exceeding 200ms for f_x=10. The large R_t case shows a first H-L back-transition at a similar time as the f_x=2.4 case.

On the right-hand-side of Fig. 4, we compare the inter-ELM target j_{sat} profiles during the time interval before and after the start of nitrogen seeding highlighted in Fig. 4(c)-(e) (the outer target of the large Rt case is not (yet) equipped with LPs). For the small f_x case, some drop in j_{sat} is observed after the seeding. However, this could, in part, be due to the limited spatial resolution of the floor LPs at these low values of f_x. For the f_x=4.4 case, where

spatial resolution is more adequate, only a weak drop in j_{sat} is apparent, with a clear peak remaining near the separatrix. The relative drop in j_{sat} is strongest for f_x=10, with the j_{sat} profile also starting to change shape. Looking at later times during the ELMy phase of the f_x=4.4 and f_x=10 cases does not show significant further changes in the j_{sat} profiles.

These discharges indicate some differences in the access to detachment with increasing f_x, with more resilience to seeding and a somewhat stronger drop in the target j_{sat} profile. In the following, we look into the region between outer target and X-point using data from multispectral imaging diagnostics on TCV (Multicam [6], MSI [25], and MANTIS [26]) and radiation measurements from bolometry.
In Fig. 5, we compare snapshots of inverted multispectral imaging data at similar times just before and during nitrogen seeding for f_x=2.4, 4.4, and 10 and for the large R_t configuration. These images correspond to data filtered at around 465.5 nm, sensitive both to CIII and NII lines. The snapshots shown correspond to time frames that did not include any ELM events. In all four cases, the emission region extends along the entire outer divertor leg and to the outer strikepoint. After seeding commences at 1.31s, the emission region recedes from the target and after only 50ms, almost all of the line emission is localized in the X-point region. The dynamics appear similar in all four cases, with the reduction in outer leg emission somewhat more pronounced in the largest f_x case. A more refined analysis of the small and large R_t cases at f_x~2, tracking the emission front position frame by frame, shows that the front movement is 20% slower for larger R_t [19].

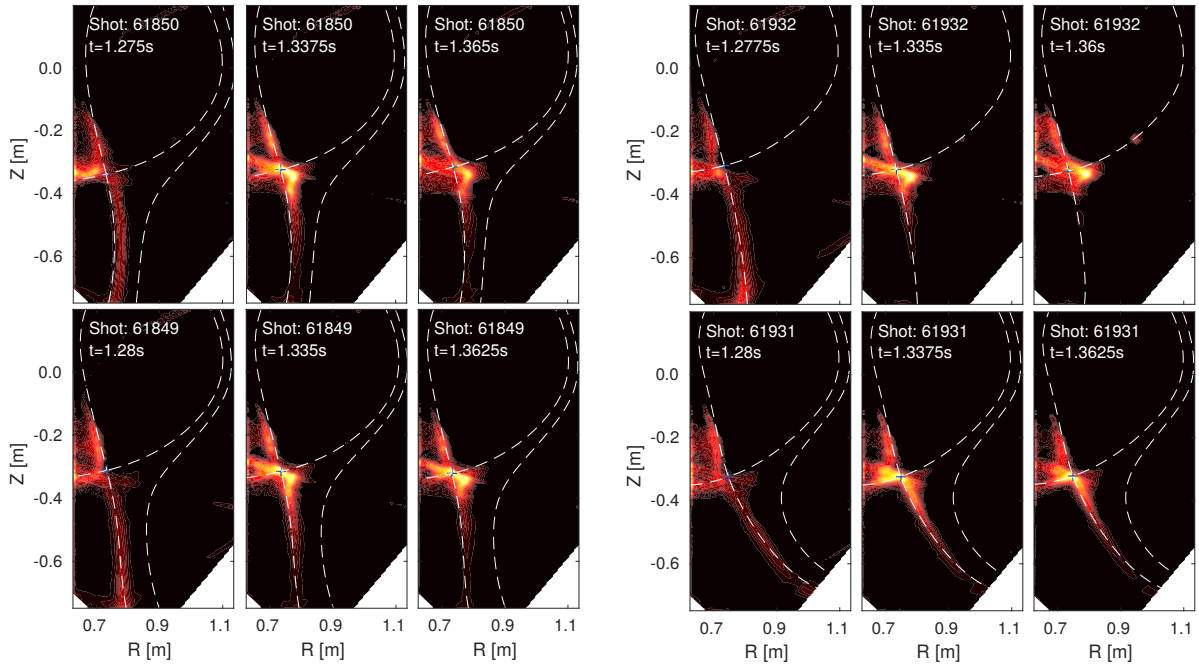

FIG 5: Inverted multispectral imaging data in the spectral range around 465.5 nm, sensitive to CIII and NII emission, in H-mode and before and shortly after the injection of nitrogen for f_x=2.4 (top left), f_x=4.4 (bottom left), f_x=10 (top right), and large R_t (bottom right). All data shown correspond to frames that did not pick up on ELMs.

A potentially important aspect of increased target poloidal flux expansion is an increased connection length and divertor volume near the target, possibly resulting in higher volumetric radiation levels. In order to experimentally assess this effect, the radiation level in the outer divertor leg is evaluated by integrating the two-dimensional emissivity determined from bolometry over the volume below z=-0.46m. This analysis is performed for a flux expansion scan in i) a density ramp in reversed field, 340kA Ohmic L-mode plasmas, ii) a nitrogen seeding ramp in the same scenario at fixed $\langle n_e \rangle = 4.4 \times 10^{19} m^{-3}$ and iii) in the nitrogen seeded, forward-field, ELMy H-mode discharges discussed in this paper. The results of this analysis are shown in Fig. 6. The bottom row shows the outer leg radiation level normalized to the input power and the top row shows the normalized radiation level in the rest of the plasma, termed here the upstream region. For the L-mode density ramp shown in the left column, the radiation in the outer leg increases first with density and then rolls over, while a steady increase in radiation is observed upstream. The leg radiation increases by approximately 50%

when scanning f_x from 2 to 21. The roll-over in the leg radiation and the increase in the upstream radiation occur later with larger f_x. This behavior is consistent with the observed reduction in the radiation location sensitivity to $\langle n_e \rangle$ with increasing f_x [3]. In the L-mode nitrogen seeding ramp, an increase in the leg radiation level with f_x is observed initially, see middle column of Fig. 6. This difference decreases with time as more nitrogen is injected, eventually disappearing. Contrary to the density ramp, the upstream radiation level increases nearly simultaneously for small and large f_x.
The same analysis for the inter-ELM times in the nitrogen seeded H-modes, right column of Fig. 6, shows also an increase in leg radiation with f_x and a similar time dependence for the upstream radiation. However, while in the L-mode cases, the leg radiation reaches approximately 15% of the input power, leg radiation is almost negligible for the ELMy cases, with values of approximately 3%. Thus, at least for the inter-ELM times, almost no power is radiated in the region where the magnetic geometry has been modified. To further assess possible benefits of increasing f_x and R_t on the H-mode detachment characteristics will likely require going to higher SOL power levels. The resulting higher divertor temperatures should allow moving the radiation region closer to the target, where magnetic geometry is modified. Higher power levels are also expected to increase poloidal gradients, leading to a more localized radiation region, possibly near the target. Beneficial for these studies will also be the divertor neutral baffles on TCV, to be installed in 2019 [27,28], which are expected to substantially increase the density of neutrals and impurities in the divertor.

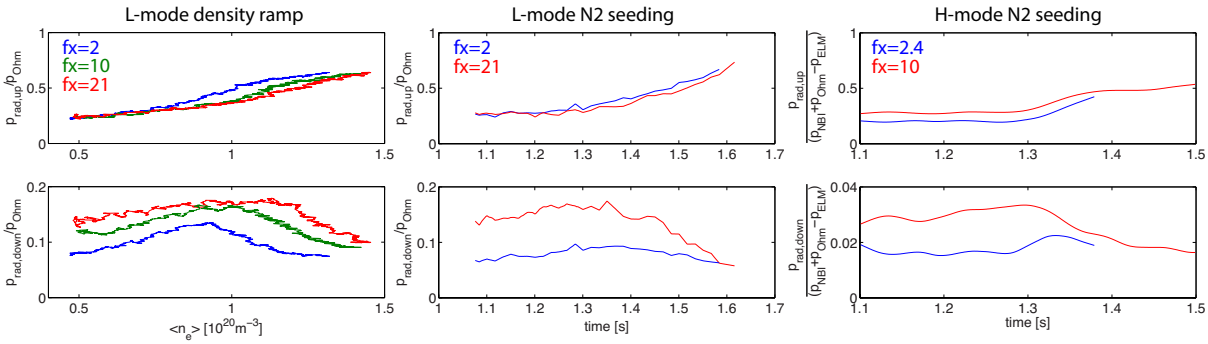

FIG 6: Comparison of radiation levels along the outer leg (z<-0.46m, bottom row) and everywhere else (z>-0.46m, upper row) for different levels of outer target flux expansion in case of density ramps in 340kA, reversed field L-mode plasmas (left), nitrogen seeding in the same L-mode plasmas at a line-averaged density of approx. $4.4x10^{19}m^{-3}$ (middle) and the nitrogen experiments in the small and large f_x ELMy plasmas discussed in this paper. Radiation levels are normalized to the input power as indicated.

4. CONCLUSIONS

Significant progress has been achieved on TCV in the understanding of transport and detachment in conventional and alternative divertor geometries. In L-mode plasmas, recent highlights include identifying the geometry dependence of divertor power sharing, heat flux width, and divertor spreading factor, diagnosing and understanding the detachment process and its modeling with SOLPS, and identifying the blob velocity regimes on TCV, the development of the upstream density shoulder, and its connection with detachment.
Significant effort has been devoted to extend detachment studies to H-mode. While the parameter space for H-mode detachment has, to date, been relatively limited on TCV, signs of nitrogen-induced partial detachment have been obtained in the inter-ELM target Langmuir probe profiles and from multispectral imaging of the divertor volume. The geometrical variations achieved so far in these ELMy H-mode plasmas consist of a scan in poloidal flux expansion by a factor 4 and an increase in outer target major radius by 40%. Increasing flux expansion indicates more resilience of the H-mode regime to nitrogen seeding and clearer signs of partial detachment, as inferred from the target j_{sat} profiles. Radiation levels in the outer divertor leg increase with flux expansion, similarly to experiments in L-mode. However, they constitute a considerably lower fraction of the input power in these H-mode cases than in L-mode. To further assess benefits of increasing flux expansion and radius near the target will likely require an increase in the radiation levels in this region. This could be achievable by increasing the SOL power levels and/or confining the neutral particles and impurities more efficiently to the divertor region by the divertor baffles, which are to be installed in 2019.

ACKNOWLEDGEMENTS

This work has been carried out within the framework of the EUROfusion Consortium and has received funding from the Euratom research and training programme 2014-2018 under grant agreement No 633053. The views and opinions expressed herein do not necessarily reflect those of the European Commission. This work was supported in part by the Swiss National Science Foundation.

REFERENCES

[1] V A Soukhanovskii, Plasma Phys. Control. Fusion 59, 064005 (2017)
[2] S. Coda et al., Nucl. Fusion 57, 102011 (2017)
[3] C. Theiler et al., Nucl. Fusion 57, 072008 (2017)
[4] H. Meyer et al., Nucl. Fusion 57 102014 (2017)
[5] H. Reimerdes et al., Nucl. Fusion 57, 126007 (2017)
[6] J. Harrison et al., Nucl. Mater. Energy 12, 1071 (2017)
[7] R. Maurizio et al., Nucl. Fusion, 58, 016052 (2018)
[8] A. Gallo et al., Plasma Phys. Control. Fusion 60, 014007 (2018)
[9] R. Maurizio et al., Nucl. Mater. Energy, submitted
[10] R. Maurizio et al., Plasma Phys. Control. Fusion, submitted
[11] N. Christen et al., Plasma Phys. Control. Fusion 59, 105004 (2017)
[12] K. Verhaegh et al., Nucl. Mater. Energy 12, 1112 (2017)
[13] K. Verhaegh et al., in preparation
[14] A. Fil et al., Contrib. Plasma Phys. 58, 746–750 (2018)
[15] A. Fil et al., in preparation
[16] N. Vianello et al., Nucl. Fusion 57, 116014 (2017)
[17] C. K. Tsui et al., Phys. Plasmas 25, 072506 (2018)
[18] O. Février et al., in preparation
[19] J. Harrison et al., in preparation
[20] F. Piras et al., Phys. Rev. Lett. 105, 155003 (2010)
[21] U. Sheikh et al, Plasma Phys. Control. Fusion, submitted
[22] A. N. Karpushov et al., Fusion Engineering and Design 123, 468-472 (2017)
[23] O. Février, Rev. Scient. Instrum. 89, 053502 (2018)
[24] B. Lipschultz et al., Nucl. Fusion 56, 056007 (2016)
[25] B. Linehan et al., Rev. Scient. Instrum., in press
[26] W.A.J. Vijvers et al., JINST 12 C12058 (2017)
[27] H. Reimerdes et al., Nucl. Mater. Energy 12, 1106-1111 (2017)
[28] A. Fasoli et al., Proc. 27th IAEA Fusion Energy Conference, Gandhinagar, India, October 22-27, 2018; paper FIP/P8-6